DAC-board based X-band EPR spectrometer with arbitrary waveform control

Thomas Kaufmann [a,1], Timothy J. Keller [a,1], John M. Franck [a,1], Ryan P. Barnes [a], Steffen J. Glaser [b], John M. Martinis [c], Songi Han [a,d,*]

[a] Department of Chemistry and Biochemistry, University of California Santa Barbara, Santa Barbara, CA, USA
[b] Department of Chemistry, Technische Universität München, Germany
[c] Department of Physics, University of California Santa Barbara, Santa Barbara, CA, USA
[d] Department of Chemical Engineering, University of California Santa Barbara, Santa Barbara, CA, USA

ABSTRACT

We present arbitrary control over a homogenous spin system, demonstrated on a simple, home-built, electron paramagnetic resonance (EPR) spectrometer operating at 8–10 GHz (X-band) and controlled by a 1 GHz arbitrary waveform generator (AWG) with 42 dB (i.e. 14-bit) of dynamic range. Such a spectrometer can be relatively easily built from a single DAC (digital to analog converter) board with a modest number of stock components and offers powerful capabilities for automated digital calibration and correction routines that allow it to generate shaped X-band pulses with precise amplitude and phase control. It can precisely tailor the excitation profiles "seen" by the spins in the microwave resonator, based on feedback calibration with experimental input. We demonstrate the capability to generate a variety of pulse shapes, including rectangular, triangular, Gaussian, sinc, and adiabatic rapid passage waveforms. We then show how one can precisely compensate for the distortion and broadening caused by transmission into the microwave cavity in order to optimize corrected waveforms that are distinctly different from the initial, uncorrected waveforms. Specifically, we exploit a narrow EPR signal whose width is finer than the features of any distortions in order to map out the response to a short pulse, which, in turn, yields the precise transfer function of the spectrometer system. This transfer function is found to be consistent for all pulse shapes in the linear response regime. In addition to allowing precise waveform shaping capabilities, the spectrometer presented here offers complete digital control and calibration of the spectrometer that allows one to phase cycle the pulse phase with 0.007° resolution and to specify the inter-pulse delays and pulse durations to ⩽250 ps resolution. The implications and potential applications of these capabilities will be discussed.

© 2013 Elsevier Inc. All rights reserved.

1. Introduction

Typically, pulsed X-band electron paramagnetic resonance (EPR) performance suffers from insufficient excitation bandwidths. The EPR spectra of nitroxide-labeled macromolecules typically span ~80 MHz when motionally averaged and up to ~200 MHz in the rigid limit at X-band [1–3]. Even a state of the art spectrometer with a 1 kW traveling wave tube (TWT) amplifier yields a 90° time on the order of 10 ns [4], which corresponds to a bandwidth that can barely excite a 200 MHz bandwidth. Furthermore, the frequency-domain excitation profile of a typical rectangular pulse is far from uniform over this bandwidth [5].

One can obtain superior control over the spin system, in particular over the excitation profile, by arbitrarily shaping the amplitude and phase of microwave pulse waveforms as a function of time. Such arbitrary waveform generation (AWG) has previously been implemented for specific, customized quantum computing applications [6,7]. Also, the NMR literature has extensively shown that arbitrarily shaped pulses can excite spins over a dramatically wider bandwidth than rectangular pulses of the same power, provide highly uniform excitation profiles [8], excite sharper spectral slices [9], as well as permit extraordinary control over even coupled spin systems [10]. In fact, it could be said that AWG pulse shaping induced a paradigm shift in NMR, and a similar impact would be expected if AWG pulse shaping in X-band EPR became widely available, versatile, and precise. Indeed, there has already been much progress in the last 1–2 years towards developing AWG-capable EPR spectrometers by modifying commercial or other pre-existing instruments [11–13].

* Corresponding author. Address: Department of Chemistry and Biochemistry, 9510, University of California Santa Barbara, CA, USA.
    E-mail address: songi@chem.ucsb.edu (S. Han).
[1] These authors contributed equally to this work.

A flexible, modular platform, as pursued in this development, that seamlessly combines the capabilities of a standard EPR spectrometer with the extensibility needed to perform precisely controlled, phase-coherent AWG would permit one to address a variety of specific issues. The ability to uniformly excite either the entire spectrum or to cleanly excite portions thereof would – in particular – benefit two-dimensional (2D) EPR and experiments involving indirect detection. These include double electron–electron resonance (DEER) [14,15], solution-state 2D electron–electron double resonance (2D-ELDOR) [16–18], and hyperfine sublevel correlation spectroscopy (HYSCORE) experiments [19,20]. These three techniques alone have demonstrated a prominent and growing importance throughout biochemistry by, respectively: providing a tool for measuring nm-scale distances and distance distributions, probing questions about the interactions between proteins and lipid membranes, and allowing one to map out the local solvent environment in glassy sample. Indeed, recent work has already shown [11] that AWG capabilities can improve the sensitivity of DEER experiments. More generally, precise excitation is a key prerequisite to enable efficient transfer through multiple coherence pathways, such as in double quantum coherence (DQC) distance measurements, which could provide potential advantages over DEER in terms of sensitivity, in the ability to probe smaller distances, and in allowing one to extract new types of geometric information [21–23]. In practice, such a sensitivity enhancement requires the ability to excite nearly all spins in a sample – here, optimized AWG pulses offer a potential route for achieving wider excitation bandwidths, while relying on amplifiers with a standard (∼1 kW) power output. Meanwhile, uniform broadband saturation would improve dynamic nuclear polarization techniques, easing data interpretation by achieving quantitative maximal saturation (s_{max} = 1) of nitroxide probes under all sample conditions—in contrast to the present situation where the maximal saturation can vary dramatically for spin labels freely dissolved in solution vs. attached to polymer chains or surfaces [24,25]. To achieve the greatest possible benefits for any of these techniques, it is important not only to implement AWG capability in the spectrometer but also to be able to seamlessly and coherently "switch on" this capability for any or all portions of a standard EPR pulse sequence. Such a seamless implementation of AWG will ultimately allow for EPR experiments whose pulse sequence evolve in active feedback with the detected signal, similar to that previously seen in laser spectroscopy [26], with shaped pulses optimized on-the-fly, allowing optimal spin rotations even in cases where certain experimental parameters might not be well characterized.

Earlier work in EPR that sought to overcome the long known limitations of rectangular pulses involved implementation of composite pulses [27], stochastic excitation [28], and tailored pulses [29]. These pulses offered more uniform excitation and improved signal-to-noise when compared to rectangular pulses; however, they still do not employ fully *arbitrary* pulse shaping capabilities and therefore did not permit *arbitrary* control over a spin system. This is only because AWG capabilities in EPR, especially at X-band frequencies and higher, remain a relatively new technology. Only within the last few years have arbitrary pulses with ns amplitude and phase resolution been investigated for X-band EPR. AWG radio frequency pulses, such as adiabatic rapid passages [30,31] or Frank sequences [32] have been shown capable of providing broadband excitation, even with limited irradiation power. Recent studies have begun to employ microwave AWG pulses and have shown promise for performing broadband EPR excitation [13], improved evaluation of dipolar couplings via DEER [11,12], dead-time reduction in high resonator quality factor (Q-factor) [33], and ultra-wideband inversion of nitroxide signals [11]. Despite these advances, relatively few spectrometers, thus far, feature arbitrary waveform generation capabilities in the X-band (8–12 GHz)

frequency regime [7,11,13,33] and many of those rely on modified commercial instruments as the main platforms [11,13]. This strategy offers the enormous benefit of allowing the user to operate within a familiar software environment, and on hardware that is already engineered to a high level of precision and verified to be fully functional. However, AWG spectrometers based on commercial instruments require integration with the commercial software, decreasing design flexibility at the current state.

A substantial amount of versatility is added if the spectrometer is home-built to be centered around a DAC (digital to analog converter) board that operates as the main control unit – a strategy primarily used in quantum computing applications [34]. This approach is necessary, for instance, if one wishes to seamlessly implement and update corrections for the resonator bandwidth and/or for amplifier saturation effects applied to the entire waveform (i.e. to all pulses simultaneously), or if one wishes to calculate the shape of an analytically specified waveform on the fly or account for variable pulse rise and fall times when calculating delays. In this study, we demonstrate that the flexibility of the design as presented here permits seamless and coherent integration of AWG capabilities into standard EPR experiments and yields entirely new opportunities. While wideband excitation has been demonstrated at X-band frequencies, most notably in the recent work by Spindler et al. [12,13] and Doll et al. [11], many applications might rely heavily on optimizing pulses that are insensitive with respect to variations in offset and/or misset of, respectively, the pulse frequency and amplitude. Therefore, it is important to explicitly demonstrate that arbitrary shaped pulses can invoke precisely the desired spin response. In this work, we map out the excitation profile of arbitrarily shaped pulses as a function of resonance offset. In the linear response regime (tip angles of <30°), this excitation profile corresponds to the frequency profile of the pulse (i.e. the Fourier transform of the pulse waveform). By analyzing the response from the spins, we can thus define a transfer function which should be independent of pulse shape and which we can subsequently use to correct the shape of various pulses, as demonstrated here for square, sinc, and Gaussian pulses. We find that we can control the shape of the pulses, *as seen by the spins*, with high fidelity.

2. Experimental

A stand-alone, home-built, AWG X-band EPR spectrometer was designed to easily and precisely manipulate the spin systems of samples that could be of biological interest. A 1 GHz digital-to-analog converter (DAC) board serves as the central control and timing unit of the spectrometer, in addition to fulfilling its primary role of controlling the amplitude (42 dB dynamic range) and phase (0.007° resolution) of an arbitrary waveform with 1 ns time resolution. The resulting pulse waveform can span a 1 GHz bandwidth that far exceeds the ∼200 MHz bandwidth of a typical nitroxide spectrum. A Python-based programming platform interacts with the spectrometer to easily program phase-coherent pulse sequences that can include square or arbitrarily shaped pulses with arbitrarily timed effective pulse lengths and inter-pulse delays.

2.1. Hardware

The YIG-tuned oscillator (Fig. 1 – #2) outputs a coherent microwave carrier between 8 and 10 GHz at 10 dBm. As described in Appendix A.1, the output frequency of this carrier is computer-controlled. This X-band carrier wave next passes through a preamplifier (MiniCircuits ZX60-183+, Fig. 1 – #3, Appendix A.1), reaching a power of 18 dBm before passing through an IQ mixer (Marki Microwave IQ-0618 L XP, Fig. 1 – #6) that shapes the amplitude and phase of the microwave waveform, which leaves the mixer
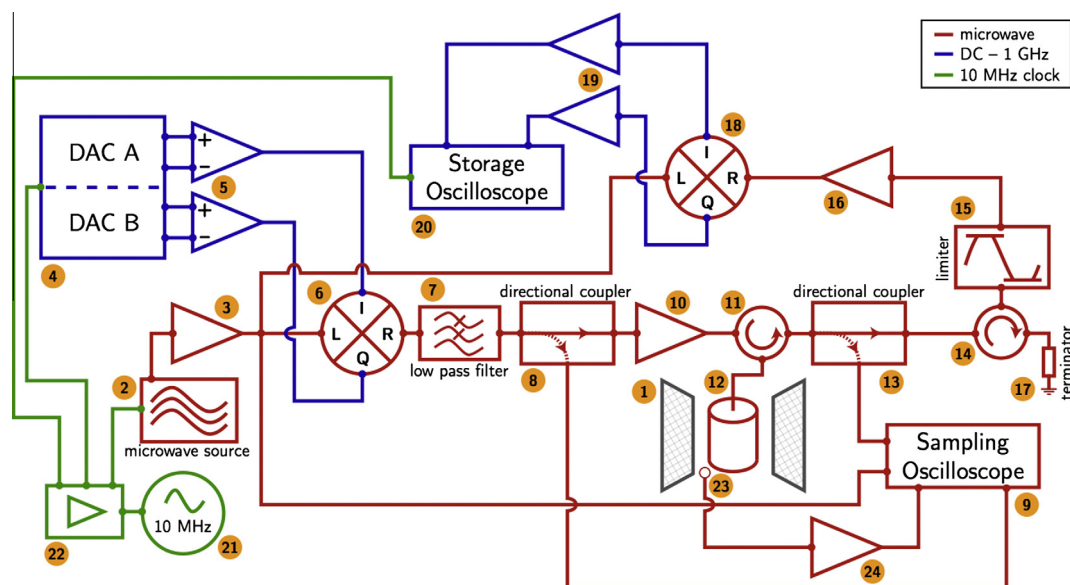
Fig. 1. Schematic overview of the pulsed AWG X-band EPR spectrometer. X-band microwave paths, indicated in red, transmit the pulse waveforms and carry the returning signal via coaxial cables, except for components #11, #13, #14, and #17, which are X-band waveguide components. The microwave carrier is generated (#2) and amplified (#3) and then mixed (#6) with two digitally controlled, quadrature 1 GHz transmit waveforms that are generated by the DAC board (#4) and amplified by two differential amplifiers (#5) to generate shaped X-band pulses at −10 dBm. The output waveform is filtered (#7), amplified to ∼43 dBm (#10), and sent to the resonator (#12). The returning signal is power-limited (#15), and amplified (#16), before being sent to a heterodyne detector comprising an IQ mixer (#18) that generates two quadrature 1 GHz intermediate frequency (IF) waveforms, which are amplified (#19) and detected by the storage oscilloscope (#20). DC to 1 GHz signal paths are shown in blue and are present in both the AWG unit and the heterodyne detector. The reference oscillator (#21) is connected to a distribution amplifier (#22) and supplies a 10 MHz signal, shown in green, which synchronizes the microwave source, DAC board, and detector. Appendix A describes the various labeled components in detail. (For interpretation of the references to color in this figure legend, the reader is referred to the web version of this article.)

at a power of about −10 dBm. The time-varied voltage (up to 10–13 dBm) modulation across the two quadrature IF (i.e. intermediate frequency) ports of the IQ mixer that define the arbitrary pulse shapes are controlled by the DAC board (Appendix A.2) with 1 ns time resolution, i.e. a 1 GHz bandwidth, (see Figs. 1 – #4 and 2). Thus, the FT of the time-domain pulse shape, i.e. the frequency profile of the waveform exiting the IQ mixer, has an arbitrarily

controlled profile in frequency space that spans ±500 MHz relative to the frequency of the carrier wave. Equivalently, the spectrometer controls amplitude and phase of the X-band pulse sequence with 1 ns time resolution.

Next, the microwave pulses are pre-amplified by 24 dB to 14 dBm (MiniCircuits ZX60-183+, Fig. 1 – #10) and further amplified by a parallel array of solid-state amplifiers (Advanced
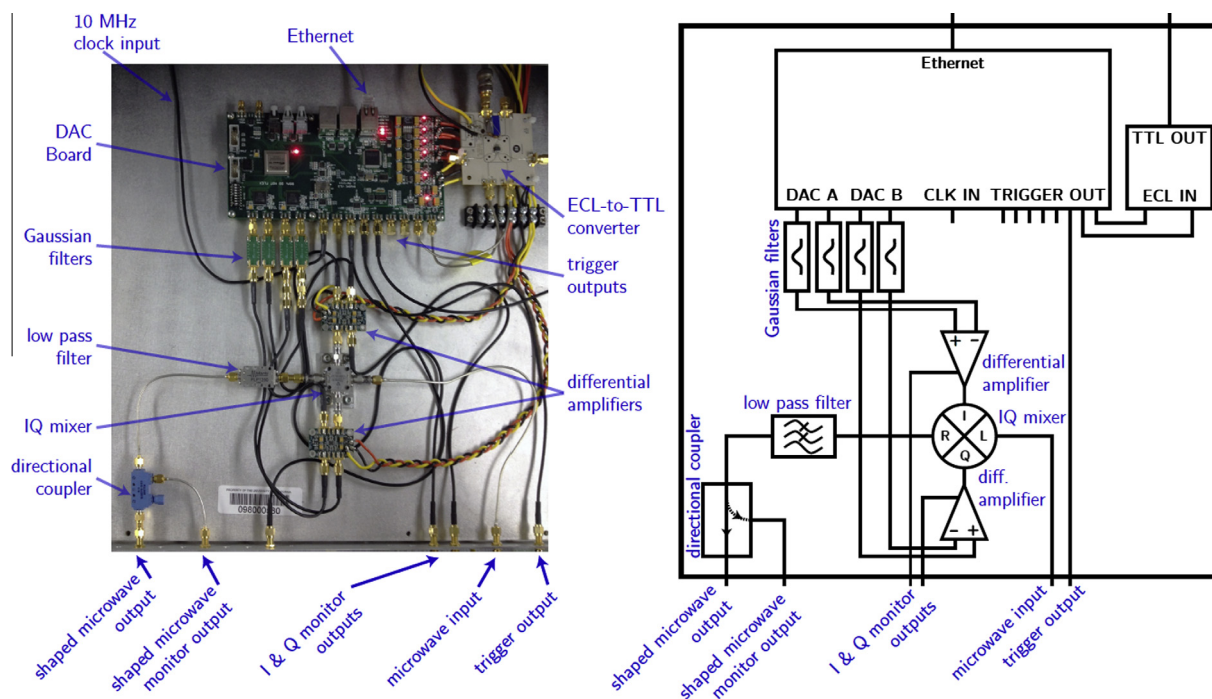

Fig. 2. Photograph and schematic of the arbitrary waveform generation (AWG) unit. The figure shows the 1 GHz digital-to-analog converter (DAC) board and the associated components used to modulate the shaped X-band waveform and to deliver a TTL timing trigger to the detector. Details are discussed further in Appendix A.2.

Microwave PA2803-24, Fig. 1 – #10, Appendix A.3) to a peak amplitude of 41 dBm (12–13 W), before traveling through a circulator (Cascade Research X-43-2, Fig. 1 – #11) into the microwave resonator (Bruker BioSpin ER4118X-MD5, Fig. 1 – #12). For all experiments here, the resonator was kept at room temperature in a static magnetic field of ∼0.35 T (Fig. 1 – #1, Appendix A.1). The circulator then directs the returning EPR signal, along with the resonator ringdown (Fig. 1 – #11), towards the heterodyne detector (Fig. 1 – #14–20). The quadrature heterodyne detector (Fig. 1 – #14–20), is a standard setup based on Rinard et al. [35], that digitizes the signal on a digital storage oscilloscope with a 1 GHz bandwidth (Agilent Technologies MSO7104B, Fig. 1 – #20). The low noise amplifier (Fig. 1 – #16) is protected from high power microwave reflections by a limiter (Fig. 1 – #15) which can tolerate short pulses from a 1 kW TWT amplifier. The recovery time of the LNA and IQ mixer are short compared to the deadtime of the spectrometer. More details are described in Appendix A.4.

In order to manipulate and detect coherent waveforms with a ∼1° accuracy in the microwave X-band phase, the system needs to consistently synchronize every hardware component that generates or detects any pulsed waveforms so that the timing between the leading edge of any trigger pulses and the crests/nodes of any carrier waves are consistent to within a jitter of ∼0.3 ps (see Appendix A.1. for phase noise values). An oven-controlled 10 MHz oscillator (Electronic Research Co. Model 130, Fig. 1 – #21) generates a clock signal and an amplifier (Stanford Research Systems Model FS735, Fig. 1 – #22) duplicate and distributes it to the DAC board (High Speed Circuit Consultants, software build 10, Fig. 1 – #4), digital storage oscilloscope (Agilent Technologies MSO7104B, Fig. 1 – #20), and YIG-tuned oscillator (MicroLambda MLSL-1178, Fig. 1 – #2). Each of the three components synchronizes to the 10 MHz clock signal via a phase-locked-loop (PLL) mechanism.

The components used to construct the spectrometer have various imperfections. Imbalances in the DAC board output levels (see Fig. 2) and imbalances in the amplitude and phase characteristics of the transmit IQ mixer (Fig. 1 – #6) lead to systematic imperfections in the amplitude and phase of the transmitted pulse waveforms, as well as a low-level bleed-through (leakage) of the carrier wave. Similar imbalances in the heterodyne detector's IQ mixer (Fig. 1 – #18) and amplifiers (Fig. 1 – #19) can lead to quadrature imbalance or DC offset in the detected signal. Rather than pursuing the task of improving the performance of each relevant hardware component, we simply implement digital calibration routines that correct for these imperfections, a strategy previously implemented by Martinis [36] for experiments on superconducting qubits. Such calibration routines require knowledge of the exact amplitude and phase of the waveform output by the AWG (i.e. output from the transmitting IQ mixer, Fig. 1 – #6). In order to avoid detector imperfections coming from the mixers, diodes, or amplifiers that constitute the home-built heterodyne detector (Fig. 1 – #14–20), we employ a sampling oscilloscope (Fig. 1 – #9), which acquires only one sample point per acquisition, but does so accurately, linearly, and with a very high (20 GHz) detection bandwidth. We stroboscopically reconstruct the amplitude and phase of the transmitting microwave waveform by feeding the sampling scope a phase-coherent (i.e. consistent to within <0.3 ps) trigger from the DAC board and an unmodulated reference signal from the microwave carrier, as described in detail in Appendix D. With knowledge of the exact microwave waveform that is transmitted, we can then calibrate for imperfections in the AWG and (by using the transmitted waveform as a known test signal) the detector, as described in Appendix C.2. While the output transfer function of the AWG system might not be significant relative to the input transfer function of the resonator (which we correct for with experiments shown in Section 3), proper calibration for the

transmitter IQ mixer's quadrature imbalance can prove crucial to one's ability to properly and easily control the pulse waveforms. This is because such imbalances are non-linear – i.e. they cannot be expressed as a matrix transformation (e.g., a scaled Fourier transform) in the complex waveform space. The Python libraries can automatically include the results of these calibrations when generating output pulse sequences or detecting the free induction decay (FID) and echo signals.

In fact, it is our core strategy that the AWG EPR spectrometer is controlled entirely through in-house Python libraries (see Appendix B.1). These allow the user to interact with the spectrometer through simple pulse programming commands that can specify the position of the various delays and timing triggers with a minimal amount of coding. The shape of the pulse waveforms can be specified either numerically or by simply writing out their analytical forms (see Appendix B.2). As Section 3 will demonstrate, there also is a distinct benefit to specifying the pulse sequence at an arbitrarily high resolution and allowing the Python library to automatically down-sample it to the 1 ns resolution of the DAC board (see Appendix C.1 for details). Similarly, a single function call allows the user to adjust the acquisition length or sampling time and to acquire signal.

2.2. Samples

The experiments presented here employed one of two samples, both of which were loaded into a 3 mm i.d. 4 mm o.d. fused quartz EPR tube (Part 3x4, Technical Glass Products, Painesville Twp., OH).

Sample A: Several flakes (∼1–5 mg) of a solid BDPA (α,γ-Bisdiphenylene-β-phenylallyl) complexed with benzene (1:1) were used without further modification (Product 152560, Sigma Aldrich, St. Louis, MO). Both, the T_1 and T_m relaxation times for this sample are approximately 100 ns [37].

Sample B: Following the procedure used by Maly et al. [37], BDPA was dissolved in toluene and then diluted in a polystyrene matrix to a concentration of 46 mmol BDPA/kg of polystyrene (Product 331651, Sigma Aldrich, St. Louis, MO). The BDPA-polystyrene-toluene paste was then dried by spreading it onto a watch glass. After sitting for 6 h, the sample was dried under vacuum overnight for 12 h. Then, 28 mg of the powdery, dilute sample was packed into the EPR tube. The T_1 relaxation time, determined by inversion recovery, was ∼5 μs, and the phase memory time, T_m, determined by spin-echo measurements, was ∼500 ns.

3. Results and discussion

In this section, we characterize the AWG X-band EPR spectrometer and demonstrate the ability to obtain the desired spin response for a given pulse. We first (Section 3.1) perform four tests to verify that this digitally calibrated single-channel spectrometer allows one to perform standard EPR experiments: (1) We characterize the phase stability and noise of the instrument. (2) By measuring the fidelity of the pulses amplified by a solid-state amplifier, we judge the spectrometer's ability to generate shaped microwave pulses at higher power. (3) Despite the absence of traditional phase-shifter components, we successfully implement standard 16-step (echo sequence) and 4-step (FID sequence) phase cycles to remove experimental artifacts, thus demonstrating precise control over the phase of our digitally calibrated pulses. (4) We perform a standard T_m relaxation measurement to test the interpulse spatial resolution achieved with the DAC board. Finally (Section 3.2), by observing the spin response over a range of resonance offsets, we obtain the frequency profile of the pulse waveforms that are seen by the spins. This allows us to correct for the

response profile of the spectrometer in order to generate rectangular, Gaussian, and truncated sinc pulses with very high fidelity.

3.1. Verification of basic spectrometer performance

To show that the various hardware components remain phase coherent, EPR signal was detected (on Sample A) with a varying number of averages, n. With perfect phase coherence, the SNR would scale linearly with $\sqrt{n}$. A $\pi/2$ rectangular pulse of 60 ns length was repeated n times at a rate of 100 kHz, yielding FIDs that were signal averaged on the oscilloscope and Fourier transformed to yield a spectrum. The SNR was determined from the integrated signal peak divided by the standard deviation of the noise. The SNR was re-determined for values of n ranging from 500 to 29,500 and plotted against $\sqrt{n}$ as shown in Fig. 3. The linear dependence of the SNR on $\sqrt{n}$ shows that the transmitter and receiver systems maintain excellent phase coherence through the course of many signal averages. Thus, the standard oven controlled oscillator that we use for our experiments has the stability necessary to perform standard pulsed EPR experiments for biochemical applications, if necessary over long timescales required to secure sufficient signal to noise.

The absolute SNR reported in Fig. 3 is not optimized to the level reported for other homebuilt or commercial X-band instruments (SNR = ~25 from 1 scan on 6.3×10^{14} total spins in a 1 kGy gamma irradiated quartz sample [38]). However, the reasons for this are well understood. First, we have not yet implemented a switch to close off the pre-amplifier (20 dB gain) and solid-state amplifier (36 dB gain), which thus presently transmit relatively high power noise to the detector. By adding a switch we expect to reduce the noise power density from the measured value of 4.1×10^{-16} W/Hz (−124 dBm/Hz) to approximately the level of thermal noise of the resonator (4.1×10^{-21} W/Hz, i.e. −174 dBm/Hz, at 300 K), and thus improve the SNR (calculated as V_{signal}/V_{rms}) by $\sim \sqrt{\frac{4.1 \times 10^{-16}}{4.1 \times 10^{-21}}} \approx 300$-fold. The loss from the resonator to the LNA in the detector is approximately 3 dB, which could be optimized. Also, the noise figure of our detection system itself (10 dB degradation in the SNR) is much higher than expected (2.51 dB) from the design previously published in [22], corresponding to another 2.4-fold gain in the (V_{signal}/V_{rms}) SNR. (A systematic diagnosis of the detection system determined that the first amplifier in the receiver train has a noise figure higher than specifications, and work is currently underway to resolve this.)

Next, we test the ease and fidelity with which our spectrometer generates a complex pulse sequence at a moderately high output power. We defined waveforms analytically at an arbitrarily high resolution (Appendix B.2) to describe a composite pulse (+x, −x, +y, −y), a triangular pulse, a Gaussian pulse, a truncated sinc pulse, and an adiabatic rapid passage sech/tanh pulse [31,39]. The Python librari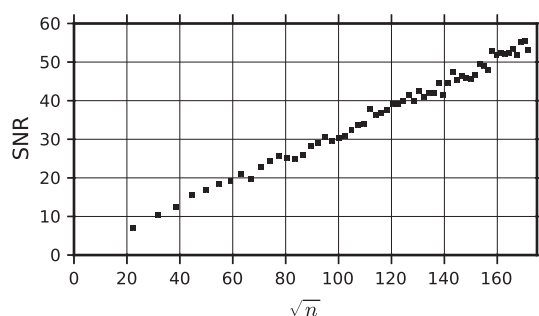es automatically calibrate (Appendix C.2) and down-sample the waveforms to 1 ns resolution to generate suitable instructions for the DAC board (Appendix C.1). The pulse sequence was captured on the sampling oscilloscope with absolute phase information after being amplified to a power of 12–13 W (41 dBm) and further calibrated using the procedure described in Appendix D. Slight deviations in pulse amplitude and phase (Fig. 4) can be seen when exceeding 70% of the maximum output power of the AWG, but are negligible at lower powers. The amplitude and phase offsets are caused by amplifier saturation which, in principle, can be corrected for separately from resonator distortions. We therefore expect that we are not limited by non-linearities present even in higher power amplifiers such as TWTs.

Next we test the ability of this spectrometer to perform standard phase cycling sequences, which are essential for pulsed EPR experiments due to their ability to select signal belonging to particular coherence transfer pathways and their ability to correct for receiver imbalances and other imperfections [40]. Some applications, in particular double quantum coherence (DQC)-based distance measurements [41], demand highly accurate phase cycling capabilities. This is typically achieved by directing the microwave pulse waveform through one of several channels with pre-set phase delays, e.g. requiring 4 channels to cycle between +x, −x, +y and −y phases. However, the spectrometer presented here implements a single channel with fully functional phase cycling that is achieved simply by adjusting the relative scaling in the two AWG quadrature inputs. Though not utilized here, this scheme offers the possibility to exploit arbitrary phase values if needed.

A Hahn echo sequence (Fig. 5(a)), with a 60 ns $\pi/2$-pulse and a 120 ns π-pulse (τ of 1000 ns), was employed to acquire signal from Sample B at a resonator Q of 1000. In order to isolate the echo signal without cycling the phase of the pulses and receiver, one must acquire an off-resonance "background scan" that is subtracted
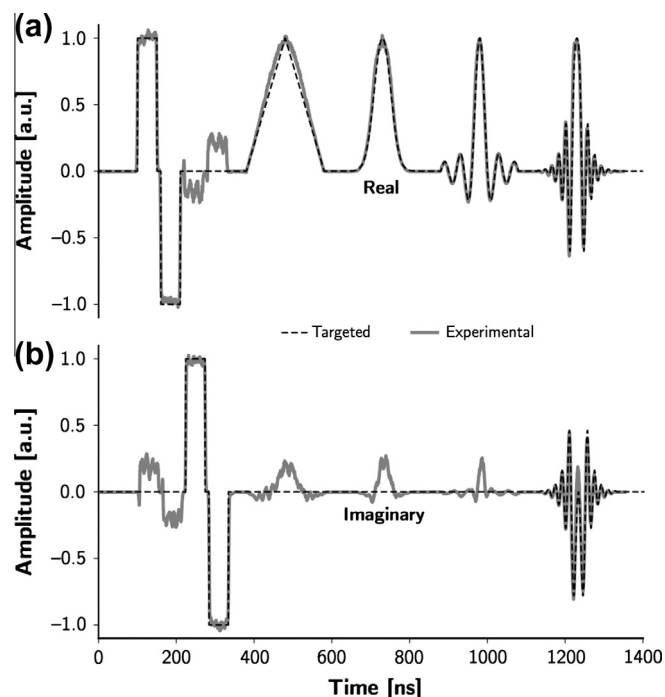

Fig. 4. Captured pulse sequence with multiple shaped pulses. Real (a) and imaginary (b) components of a targeted waveform (black dashed lines) are compared to the microwave waveform captured on the sampling oscilloscope (gray, solid lines) following the procedures described in Appendices C.1, C.2, and D. The target waveform consists of a sequence of composite pulses, a triangular pulse, a Gaussian pulse, a truncated sinc pulse, and a sech/tanh adiabatic rapid passage (left to right, respectively).
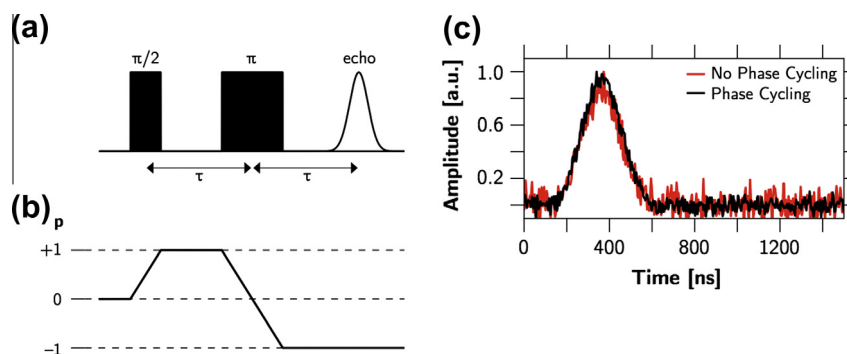

Fig. 3. Signal coherence test. SNR, calculated as explained in the text, as a function of $\sqrt{n}$, where n is the number of scans that are averaged.

Fig. 5. Hahn echo measurement verifies functionality of AWG-based phase cycling. Hahn echo pulse sequence (a) and respective coherence transfer pathway (b), as well as comparison of the signal (c) retrieved with off-resonance background subtraction (red) vs. a 16-step phase cycle (black) appropriate for the coherence pathway shown in (b). A 400 MHz digital band-pass filter was applied to the signal shown in (c). The SNR (integrated echo intensity vs. RMSD of the noise) is 9.6 for off-resonance background subtraction and 18.4 for phase cycling. (For interpretation of the references to color in this figure legend, the reader is referred to the web version of this article.)

from an on-resonance signal. We performed such an experiment for comparison. Then, we carried out experiments using a 16-step phase cycle that selects the coherence transfer pathway of the echo (Fig. 5(b)) to remove any spurious pulse ring-down signal and DC offset, as well as unwanted residual FID signal, from the second pulse without the need for a background scan. As expected and shown by Fig. 5(c), both background subtraction and phase cycling yield clean, identical echo signals, while the SNR of the phase cycled result is approximately twice as large when the same number of total scans are used for both methods. This SNR improvement is expected since half the scans for the background subtraction experiment were acquired off-resonance, resulting in half the signal amplitude.

In the case where we are collecting an FID, phase cycling no longer offers the same advantage in removing the ring-down from the signal. However, it is well known that phase cycling can effectively eliminate instrumental imperfections. For instance, if the two quadrature detection channels are not precisely 90° out of phase with each other or have different sensitivities, a negative frequency mirror peak appears in the Fourier transform of the FID [42]. As shown in Fig. 6, when an FID signal is acquired with a 4-step phase cycle, the phase cycling provided by the spectrometer successfully removes the artifactual mirror peak that occurs in the Fourier transform of the FID. Along with the previously demonstrated selection of the echo signal, this demonstrates the precision and stability of the mixer-based, digital AWG phase cycling method, which does not require separate pre-set phase delay channels.

Many home-built spectrometers offer a timing resolution significantly better than 1 ns [11,43]. Such high timing resolution might be needed in the currently presented spectrometer for select

experiments, especially after upgrading the amplifier to a high power TWT. Since the fundamental timing resolution of the AWG presented here is only 1 ns, a concern might arise over how well this spectrometer can control inter-pulse spacing or calibrate the pulse lengths with sufficient precision. However, while the 1 ns time resolution of the DAC board fundamentally limits the bandwidth of the pulses in frequency space (and therefore limits the sharpness of the edges of the pulses), the pulse lengths and inter-pulse delays can still be defined with a time resolution finer than 1 ns. This can be accomplished by defining the desired waveform at an resolution, such as 10 ps, where the inter-pulse delays and lengths are defined with a resolution that is intentionally higher than that achievable with the DAC board. This high resolution waveform is then convolved with a 1 ns Gaussian, filtering out frequency components outside the bandwidth of the DAC board, while preserving a high dynamic range that finely defines the pulse amplitude. Then, the pulse is converted to the resolution of the DAC board by reducing the bandwidth in frequency space to 1 GHz to match the bandwidth of the DAC board.

This "down-sampling" procedure makes use of the large dynamic range of the DAC board to preserve the distance between the centers (or edges) of the pulses with a resolution of better than 250 ps, as Fig. 7 experimentally demonstrates.

To conclude this section, we present a proof-of-principle EPR experiment that implements both sub-ns changes in delay times and phase cycling. We employ a phase-cycled Hahn echo pulse sequence (as in Fig. 6(a–b)) to acquire signal from Sample A at a resonator Q of 500 and $\pi/2$ length of 60 ns. Here, the delay time, τ, between the $\pi/2$- and the π-pulse was varied to carry out measurements of phase decoherence (i.e. measurement of T_m)
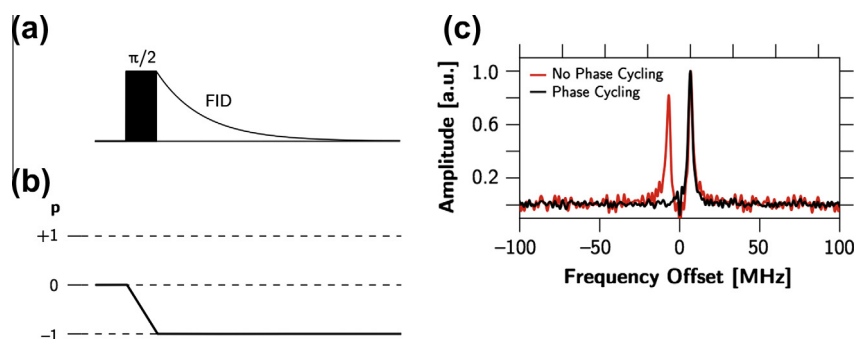

Fig. 6. FID measurement verifies functionality of AWG-based phase cycling through removal of receiver imbalance artifacts. FID pulse sequence (a) and coherence transfer pathway (b). Fourier-transform of FID with magnetic field set 2.4 G off-resonance (c). The negative frequency peak due to receiver imbalances is successfully eliminated with a digitally calibrated, mixer-based phase cycle.
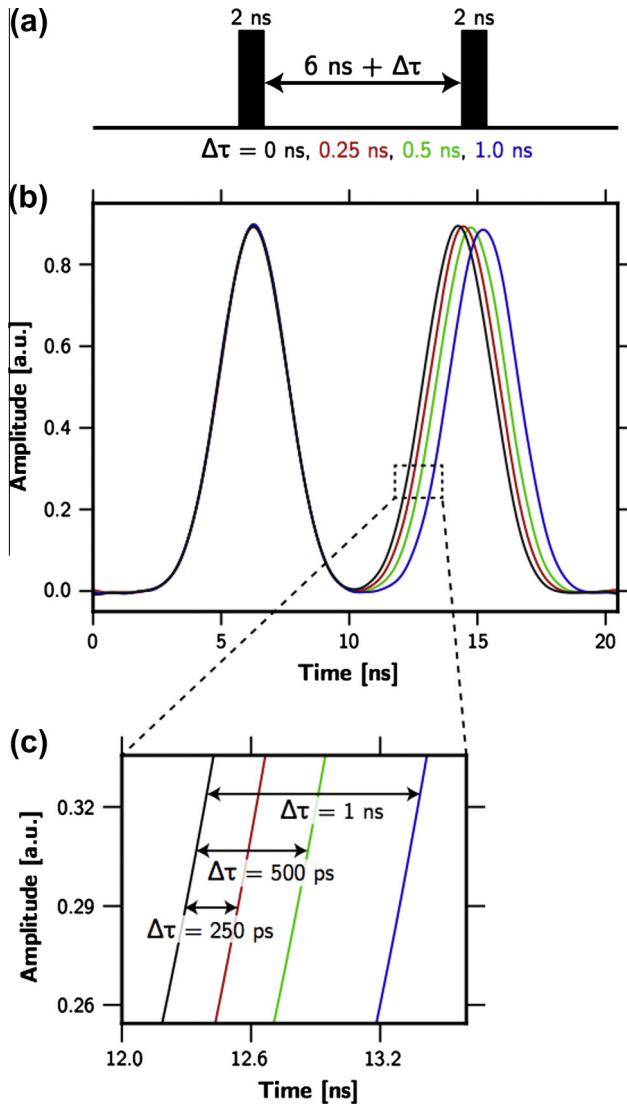
(a) 2 ns   2 ns

6 ns + Δτ

Δτ = 0 ns, 0.25 ns, 0.5 ns, 1.0 ns

(b)

(c)

Δτ = 1 ns

Δτ = 500 ps

Δτ = 250 ps

Fig. 7. Pulse sequence showing delays that are defined with ⩽250 ps time resolution. The pulse sequence (a) consists of two 2 ns wide pulses with a varying inter-pulse delay of 6 ns, 6.25 ns, 6.5 ns, and 7 ns and generates a microwave waveform (b) that is captured on the sampling oscilloscope (as described in Appendix D) and digitally filtered with a 1 GHz bandpass. As the higher resolution inset (c) shows, delays with ⩽250 ps resolution are generated with high fidelity.

and signal was acquired with 5000 averages (Fig. 8). The best-fit exponential decay determined the T_m relaxation time to be 490 ± 14 ns. Fig. 8 (inset) shows the same measurement at a 250 ps resolution in τ. This higher resolution data smoothly interpolates between the lower resolution points, closely following the best-fit exponential decay. We thus find that AWG-based systems offer the benefit of observing the spin-echo relaxation decay with nearly unprecedented time resolution. This should allow one to determine subtle features in T_m, such as those coming from multiple overlapping relaxation contributions [37], with high precision and also to resolve short decay times. Although we are limited by the rising and falling edges when generating short pulses, we can specify the length of a pulse to within 250 ps by our downsampling procedure, in a similar way to finely tuning the delay length. In situations where longer pulses are required, such as matched pulses in ESEEM which have been shown to increase modulation depth by an even order of magnitude in some cases [44], we can provide precise tip angles in the case of constant B_1 amplitude.
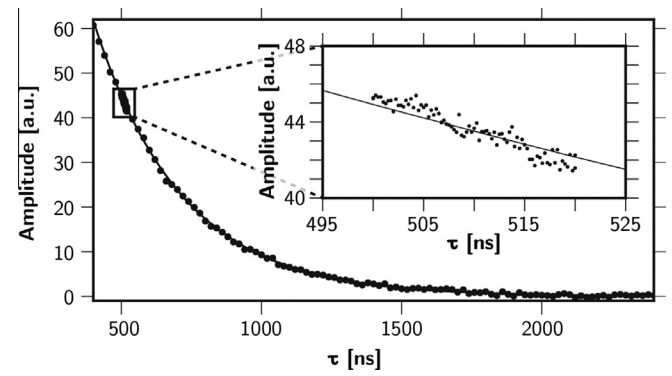

Fig. 8. T_m relaxation curve with 250 ps step size. This figure presents a T_m relaxation curve recorded from a Hahn echo sequence on Sample B. A 12 MHz digital bandpass filter was applied to the data and the echo area was integrated and plotted against the delay time, τ, between the pulses, which was varied in 34 ns steps. The solid black line (in both the main plot and inset) gives the exponential fit of this data, with $T_m = 490 \pm 14$ ns. The inset shows the same measurement, acquired with higher time resolution; for this data, a 250 ps step size was used for the pulse delay.

3.2. Spin response to transfer function corrected pulses

The AWG capabilities of the spectrometer presented here allow us to generate any arbitrary pulse shape as part of a coherent pulse sequence. However, the pulse waveform that acts on the spins inside the cavity does not exactly match that leaving the AWG. In previous studies, a pickup coil has been used to monitor the microwave waveform inside the cavity. However, the pickup coil can introduce unknown spatial distortions to the microwaves inside the cavity and also subjects the measured waveform to its own transfer function, which may not be consistent for all setups. Therefore, we instead directly monitor the spin response from a sample with a narrow linewidth, which selects the amplitude of a narrow spectral slice of the excitation profile of the pulse. By sweeping the field, we map out the excitation profile of the pulse as a function of resonance offset. This technique allows us to verify and optimize precise control of the waveform seen by the spins.

The pulse is convolved in the time-domain with an impulse response function that depends on the resonator Q-factor, residual miscalibration of the final AWG output, and additional group delays and imperfections from the transmission lines (to name some of the most obvious sources):

$$y(t) = x(t) * h(t) = \int_{-\infty}^{\infty} h(t-\tau)x(\tau)d\tau \qquad (1)$$

Here $x(t)$ is the waveform of the programmed pulse, $y(t)$ is the waveform of the pulse inside the resonator, and $h(t)$ is the impulse response function. In the frequency domain, the convolution above is equivalent to a multiplication, i.e.:

$$\mathcal{F}\{y(t)\} = \mathcal{F}\{x(t)\}\mathcal{F}\{h(t)\} \qquad (2)$$

or

$$Y(f) = X(f)H(f) \qquad (3)$$

where the functions $Y(f)$, $X(f)$, and $H(f)$, are Fourier transforms of $y(t)$, $x(t)$, and $h(t)$, respectively.

We directly obtain the experimental excitation profile, $Y(f)$, by reading out the spin response in the linear response (i.e. small tip angle) limit. We can then determine the frequency-domain transfer function, $H(f)$, of the spectrometer system as

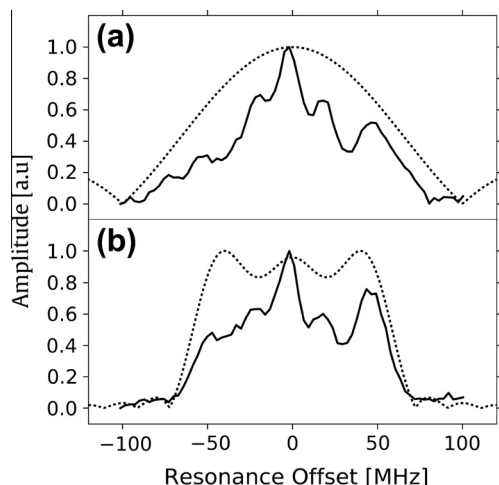$$H(f) = \frac{Y(f)}{X(f)} \qquad (4)$$

Fig. 9. Spin response to broadband pulses. The spin response from (a) 10 ns square and (b) 50 ns truncated sinc pulses used to calculate the resonator transfer function. The solid lines (–) illustrate the experimental excitation profiles and the dashed lines (⋯) illustrate the Fourier transform of the output pulse waveforms. The transfer functions – calculated from the ratio of the experimental excitation profile and Fourier of the pulse waveform – for (a) and (b) are in good agreement.

We can then define a corrected pulse, $x'(t)$, whose Fourier transform is $X'(f)$,

$$X'(f) = \frac{X(f)}{H(f)} \qquad (5)$$

which experimentally yields the frequency response of the desired waveform, i.e. $Y'(f) = X(f)$, where $Y'(f)$ is the frequency profile seen by the spins:

$$Y'(f) = H(f)X'(f) = X(f) \qquad (6)$$

Thus, when the AWG generates the corrected pulse, $x'(t)$, the waveform inside the cavity, $y'(t) = F^{-1}\{Y'(f)\}$, will now match the target waveform, $x(t)$. Thus, by determining and correcting for

the transfer function, $H(f)$, one can arbitrarily control the waveform, $x(t) = y'(t)$, seen by the spins inside the resonator. Note that the transfer function, as defined above, would also include distortions due to frequency-dependent detection sensitivity, therefore, for greater accuracy, we could include the detector frequency response.

As a proof of concept, we seek to show that this spectrometer can arbitrarily tailor the excitation profiles of pulses over a 60 MHz bandwidth. To start with, the transfer function of the spectrometer system must be determined over a broad bandwidth relative to the corrected pulses. Therefore, the excitation profile of a short 10 ns rectangular test pulse (∼10° tip angle) was determined (Fig. 9(a)). The magnetic field was swept over a range of ±35 G (with 1 G resolution) around the resonant magnetic field, while the FID of a BDPA sample (FWHM = 1.4 G) was recorded. The FID was Fourier transformed, and the integrated signal amplitude (60 MHz integration width) was plotted against the resonance offset (converted from field using g = 2.00). To calculate the transfer function, $H(f)$, we divide the experimental excitation profile, $Y(f)$, by the Fourier transform of the pulse, $X(f)$ (Eq. (4)). Because the Fourier transform of the 10 ns rectangular test pulse first crosses zero only at ±100 MHz, the excitation profile of the test pulse presents significant signal amplitude over the 60 MHz bandwidth of this experiment. Therefore, we can accurately determine the transfer function over the bandwidth of this experiment. To verify that the transfer function is independent of the pulse shape, we repeated this procedure with a 50 ns truncated sinc pulse as the test pulse (Fig. 9(b)). As expected, the resulting transfer function was in reasonable agreement with that from the 10 ns rectangular test pulse.

We applied the transfer function to correct three different pulse waveforms – rectangular, Gaussian, and truncated sinc – in order to verify a subsequently increased control over the spin system. The rectangular pulse was 100 ns long. The sinc pulse with the same maximum power was truncated after the 2nd side lobe and was adjusted to a length of 250 ns so that it yielded similar signal amplitude. The Gaussian pulse was 250 ns long with a FWHM of 88 ns and also featured the same peak power and signal amplitude.
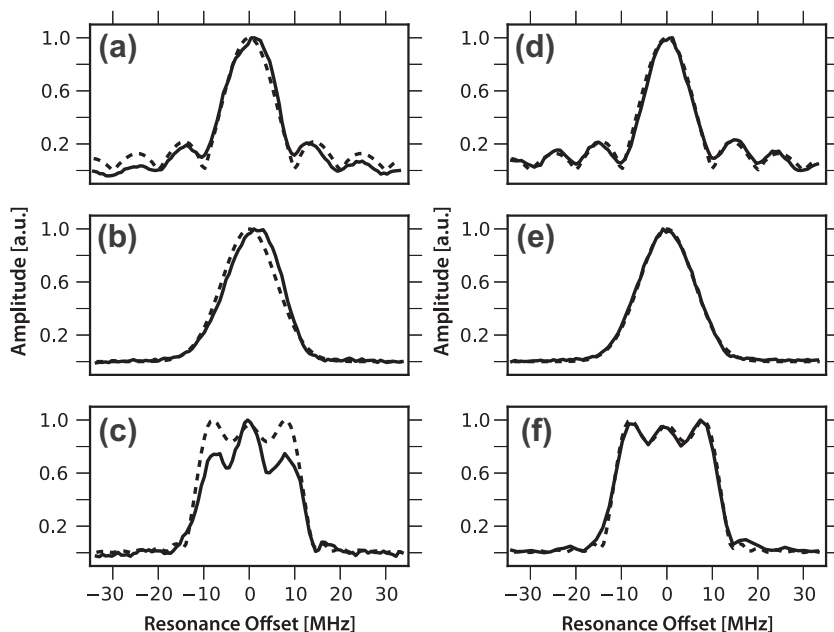

Fig. 10. Spin excitation profiles resulting from shaped pulses. Normalized spin excitation profiles (solid lines) generated by a rectangular (a), Gaussian (b), and truncated sinc (c) pulses, acquired as described in the text. The analogous transfer function corrected pulses for (a–c) are shown in (d–f), respectively. The dashed lines show the Fourier transforms of the excitation pulses as generated by the AWG, which represent the excitation profiles of the pulses predicted by the small tip angle approximation (which is valid for these measurements), whereas the solid lines show the experimentally measured excitation profile of the spins as a function of resonance offset.
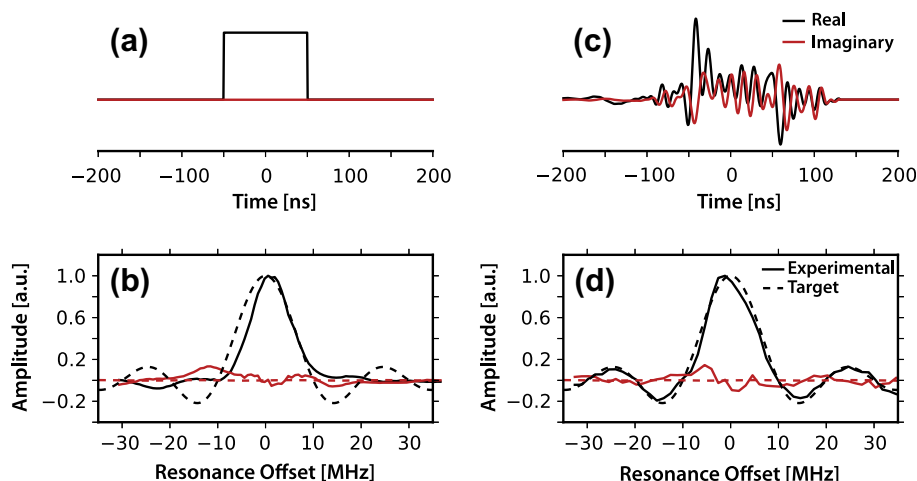
Fig. 11. Phase sensitive transfer function correction for square pulse. Black and red lines represent real and imaginary part, respectively. For excitation profiles, solid (-) and dashed (- -) lines represent experimental and target excitation profiles, respectively. (a) Time-domain 100 ns square pulse. (b) Spin response to 100 ns square pulse. (c) Complex transfer function corrected pulse. (d) Spin response to complex transfer function corrected pulse. As before, excitation profiles were collected using pulses in the linear response (i.e., small tip angle) regime. (For interpretation of the references to color in this figure legend, the reader is referred to the web version of this article.)

The excitation profiles were mapped out with sample A as shown before, except the magnetic field was swept over a narrower range of ±12 G in steps of 0.25 G. When not performing the transfer function correction, the 24 MHz bandwidth of the resonator ($Q = 400$) attenuates the side features of the excitation profile (Fig. 10). This is especially apparent for the rectangular (a) and sinc pulses (c). As expected, once we apply the transfer function correction (d–f), the detected excitation profile matches the Fourier transform of the desired pulse with very high fidelity (Fig. 10).

The transfer function corrected excitation profiles shown in Fig. 10 were obtained by defining an absolute value transfer function and contain no phase information. If instead, we define a complex transfer function, we can correct both the real and imaginary parts of the excitation profile – corresponding to the X and Y components of magnetization in the rotating frame. A square 100 ns pulse was sent to the microwave resonator, which was overcoupled to a Q of ∼500. As indicated by the excitation profile Fig. 11(b), the pulse is significantly distorted by the bandwidth of the resonator and by imperfections in the various transmission line components (i.e. waveguides, circulator, etc.). After the complex transfer function correction, the corrected pulse is significantly different from the original square pulse Fig. 11(c). The transfer function correction makes the pulse more broadband, thus introducing new frequency components that cause oscillations in the waveform of the pulse. These oscillations also indicate that the transfer function of the resonator is not as intuitive as the Lorentzian-shaped response function that is predicted by an RLC circuit-like model. Additionally, the small amplitude peaks at the beginning and end of the pulse can be accounted for by noting that they help compensate for the finite rise and fall time inherent to the resonator, i.e. these peaks force the resonator to charge and de-charge, respectively. Once the complex transfer function is applied to the original pulse, both the real and imaginary parts of the excitation profile are significantly improved. Remarkably, despite being initially highly attenuated, after correction, the off-resonance features are scaled properly, as given by Fig. 11(d), where they closely match the target excitation profile (100 ns square pulse).

Thus, to support our claim of coherent control over a spin system, we have demonstrated control over the phase of the excitation profile. In other words, The DAC board-centered spectrometer can generate arbitrary pulse sequences phase coherently. Coherent excitation is necessary not only for proper phase cycling, but is also a prerequisite for transferring polarization through multiple quantum coherence states. Both of these are fundamental for performing double quantum coherence distance measurements, which with arbitrarily shaped pulse sequences can be done in an optimized manner or for any other pulse sequence that relies on coherence transfer. It should be noted that although we have obtained good agreement between the target and experimental excitation profiles, these experiments were done with relatively long pulse lengths and narrow bandwidth samples, where the experimental opportunities should be fully explored by transitioning to high-power amplifiers.

4. Conclusion

With this work, we demonstrate precise control over the spin system in standard pulsed EPR experiments – achieved with an X-band AWG EPR spectrometer, entirely home-built around a DAC platform as the main control unit. In particular, we precisely shape the offset-dependent response of the spins to follow a variety of different excitation profiles. The spectrometer presented here thus overcomes the limitations of rectangular pulses by enabling truly arbitrary waveform capabilities for pulsed EPR. At the same time, it represents an alternative approach to spectrometer design. Arbitrary control over the phase and amplitude of the pulses, as well as the timing of all spectrometer components are combined into one digital control unit. This provides the technical capability for generating precisely controlled and optimized coherent pulse sequences, dramatically decreasing the complexity of the instrument and allowing for a detailed level of control and ability to further optimize the instrument. A Python-based interface easily masks the complexity such instrumentation might otherwise introduce, by allowing the user to program the instrument as though controlling a standard pulse sequence with an arbitrarily high resolution and permitting the user to specify pulses inline using analytical descriptions of the relevant functions. Down-sampling to the intrinsic DAC bandwidth and various calibrations are handled automatically and "behind the scenes" within the Python-based interface. Thus, we believe this control system offers significant advantages over what is currently available as state-of-the-art platforms for pulsed EPR spectrometers.

Similar to other recent work [11,13,33], we find that a design based on mixing a shaped intermediate frequency wave with a higher frequency carrier proves to be extremely versatile and practical. In particular, we note that the carrier frequency can be changed without the need to recalculate the entire waveform. This

setup could also be directly adapted to several other frequency bands, including K-band (18–26.5 GHz) and Q-band (33–50 GHz), simply by replacing the X-band-specific components (the microwave source, mixer, and the microwave resonator and bridge components). The only limitation for applying the same AWG technology to much higher frequencies is that the intrinsic 1 GHz bandwidth would no longer cover the bandwidth of the resonator; however commercial DAC boards that operate at higher bandwidths are already available [11,45], and, with more effort, the design of the present DAC board could be scaled to a faster sampling rate and subsequently higher bandwidth. Furthermore, even in wideband EPR spectrometers without resonators or with low-Q resonators, where power becomes the main factor limiting excitation bandwidth, experiments should substantially benefit from the enhancement in excitation bandwidth provided by arbitrarily shaped pulses.

This work contains similar developments to those by Spindler et al. [12,13] and Doll et al. [11] that have implemented add-on AWG units to pre-existing X-band EPR spectrometers, and have developed techniques to correct for the response of the resonator as well as the non-linear response of the TWT amplifier. In this study, we have investigated the fidelity of the excitation profiles of arbitrarily shaped pulses. As more advanced AWG EPR experiments are developed, the precision of the arbitrary pulses will become increasingly important and a necessary consideration in generating multiple quantum coherence pulse sequences.

Further improvements can capitalize on the advances presented here. Optimization procedures and on-the-fly feedback techniques can be implemented in this design to improve the excitation profiles. This work was performed on narrow bandwidth samples at relatively low microwave powers. Thus, integrating a high-power TWT into this setup is required before AWG capabilities are demonstrated to become truly advantageous over standard EPR techniques. A high-power TWT would allow one to implement the same level of high-fidelity control, while exciting spins over a significantly larger bandwidth. By allowing one to excite significant signal amplitudes from fast-relaxing samples, it would also allow one to take advantage of the 250 ps resolution in pulse length and delay timing to acquire highly resolved relaxation measurements. This would be of great and direct benefit to characterize fast relaxing samples (i.e. samples with a short T_m or T_1), such as found with many nitroxide labels or transition metal probes under ambient conditions, and are relevant for many biological applications. At high power, one should be able to implement very similar methodologies to those presented here. The shape of the waveforms seen by the spins can still be directly mapped out in the linear response regime to verify reproduction of the exact waveform desired. Then (with appropriate correction for any amplifier nonlinearities), the power could be scaled up into the regime of nonlinear spin response to generate a variety of interesting effects [46]. In fact, the sampling-scope detection scheme presented here should allow one to measure and thus correct for a significant portion of the nonlinear distortions generated at high powers, near the saturation point of the TWT, thus easily allowing for the types of nonlinear corrections that have been implemented by Spindler et al. and Doll et al. [11,13]. Therefore while offering flexibility, control, and ease of use at X-band, it is of significant value that this spectrometer platform design can successfully shape the excitation profiles of the spins – in fact matching the theoretical profiles with fidelity beyond our expectations, and thus promising significant improvements for a variety of EPR measurement techniques.

Acknowledgments

Appendix A. Hardware

A.1. Magnet and microwave source

A schematic overview of the spectrometer is shown in Fig. 1 in the main text. A field controller (Bruker ER 032M) controls the 0.35 T static field generated by the electromagnet (Bruker ER 070, Fig. 1 – #1). A YIG-tuned oscillator (MicroLambda MLSL-1178, Fig. 1 – #2) generates a low-phase-noise (-53 dBc/Hz at 100 Hz offset, -60 dBc/Hz at 1 kHz offset, -93 dBc/Hz at 10 kHz offset) + 10 dBm cw X-band sine wave, which is split, with one channel pre-amplified (MiniCircuits ZX60-183+, Fig. 1 – #3) to 18 dBm and fed into the home-built AWG unit (Fig. 2) and the other channel sent to the heterodyne receiver (Section A.4). Communication with the field controller occurs through a GPIB connection; a GPIB-Ethernet Controller 1.2 by Prologix, LLC allows the Python library to communicate with this and all other GPIB devices through a TCP/IP socket. The microwave source is computer controlled with a USB interface (FTDI FT245R embedded in the UM245R development board) together with the FTDI D2XX drivers that allow direct access to the device in the "bit-bang" mode, which permits one to set the voltage levels on the various pins simultaneously. Both the static field and microwave frequency can be set from a Python script, which can also read out the current Hall probe reading and whether or not the microwave source is currently phase-locked.

A.2. AWG unit

The AWG unit is comprised of a two-channel 1 GHz DAC board (High Speed Circuit Consultants, software build 10, Fig. 1 – #4), [36] four Gaussian filters (High Speed Circuit Consultants) that reduce output noise, two differential amplifiers (Fig. 1 – #5) that drive the I and Q channels of an IQ mixer (Marki Microwave IQ-0618, Fig. 1 – #6), a low pass filter (Marki Microwave FLP-1250, Fig. 1 – #7) that suppresses harmonics generated by the IQ mixer, and a directional coupler (Fig. 1 – #8) that allows monitoring of the shaped microwave output of the AWG unit with 10 dB of attenuation on a sampling oscilloscope (Tektronix 11801C, Fig. 1 – #9) with two sampling heads (Tektronix SD 24, Tektronix SD 22), as described in Appendix D. Additionally, each of the two differential amplifiers has a secondary output that can be monitored on a standard digital storage oscilloscope.

The DAC board was developed by John Martinis at UCSB [36] in collaboration with Steve Waltman (High Speed Circuit Consultants), and features two differential (i.e. two port) outputs with a 14 bit (i.e. 42 dB) dynamic range and 1 ns time resolution. The memory of the board allows for storage of up to 16 μs long waveforms. Additionally, parts of the pulse sequence can be called independently and delays of arbitrary lengths can be inserted. The bandwidth limitation of the AWG unit is set by the I and Q inputs of the IQ mixer, which feature a bandwidth of 500 MHz and thus make the IQ mixer the bandwidth limiting component in the setup. A significant advantage over commercially available AWGs is that the DAC board provides four differential ECL trigger outputs that

can be utilized to control other components of the spectrometer. For this spectrometer, an ECL-to-TTL converter was built (ON Semiconductor ECLSOIC8EVB and MC100ELT21) to open and close the gate of a TWT amplifier. Another ECL trigger output triggers the sampling oscilloscope as well as the oscilloscope connected to the heterodyne receiver. Thus, the DAC board not only controls the phase and shape of the microwave pulses, but also functions as the central timing unit. The FPGA-based design of the DAC board also allows for custom modifications of its functionality, if desired.

A.3. Microwave transmission

The shaped pulse output of the AWG, approximately −10 dBm coming out of the mixer, is pre-amplified (MiniCircuits ZX60-183+) by 24 dB and further amplified (Fig. 1 – #10) by either a 1 kW traveling wave tube (TWT) amplifier (Applied Systems Engineering Model 117), which we measured to have a gain of 60 dB and a P1dB of 61 dBm, or an array of four solid-state amplifiers. The four amplifiers (Advanced Microwave PA2803-24) each yield a gain of 30 dB (P1dB 35 dBm each) and are adjusted with phase shifters to yield coherent outputs that are combined for a net gain of 36 dB to reach a maximum power of approximately 12–13 W of power (41 dBm). Specifically, the array of solid-state amplifiers uses 3 splitters (MiniCircuits ZX10-2-126) to dividethe signal into 4 pathways, 3 phase shifters (Aeroflex Weinschel 980-4) to adjust the phase of 3 of the pathways to match the first one, before the signal is fed into the 4 amplifiers, and 4 isolators (UTE Microwave, CT-5450-OT) to protect the amplifier outputs from reflections before the 4 pathways are combined (Narda Microwave 4326-4) again. The amplifiers are powered by a linear power supply (Protek 18020M), mounted on a thick aluminum block and additionally cooled by computer fans. A 4-port circulator, with port 4 terminated (Cascade Research X-43-2, Fig. 1 – #11), directs the microwave pulses to the resonator (Bruker ER4118X-MD5, Fig. 1 – #12) that holds the sample and returns the reflected signal to the detector.

For the purposes of monitoring the system, a directional coupler (Fig. 1 – #13) directs −20 dB of reflected signal to the sampling oscilloscope. A second directional coupler, placed in front of the YIG-tuned source (Fig. 1 – #2), directs −20 dB of the X-band carrier wave to the second channel of the sampling oscilloscope, where it is used as a reference to determine the reflected microwave signal with absolute phase information as outlined in Appendix D.

A.4. Microwave detection

The microwave signal returning from the resonator is sent to a 3-port circulator (Cascade Research X43-10-1, Fig. 1 – #14) and from there to a PIN-diode limiter (Aeroflex ACLM-4571FC31 K, Fig. 1 – #15), which protects the low-noise amplifier (Miteq AMF-3F-09001000-13-8P-L-HS, Fig. 1 – #16) from damage due to high power microwaves. The aforementioned circulator (Fig. 1 – #14) directs any microwave power reflected from the limiter into a high-power terminator (Fig. 1 – #17).

To obtain heterodyne detection, the amplified signal and the output of the microwave carrier are input into another IQ mixer (Marki Microwave IQ-0618, Fig. 1 – #18), generating two IF (i.e. intermediate frequency) signals in quadrature, which have a frequency range between DC and 500 MHz. These signals are amplified by two amplifiers (MiniCircuits ZFL-500+, Fig. 1 – #19) and detected with a (time-base) digital storage oscilloscope (Agilent Technologies MSO7104B, Fig. 1 – #20) or a high speed digitizer card (Agilent Acqiris 1082A).

Appendix B. DAC board control software

B.1. DAC board communication

To control the DAC board from a Python platform, the following software is needed:

- LabRAD Manager.
- LabRAD Direct Ethernet Server.
- LabRAD GHz FPGA Server.
- LabRAD Registry Editor.
- Python 2.6 or 2.7.
- Pylabrad.
- Pyreadline.
- Pywin32.
- SciPy.
- Twisted (www.twistedmatrix.com).
- Numpy.
- iPython.
- Matplotlib.

The LabRAD components, basic scripts to run and control the DAC board as well as an initial set of registry keys for the LabRAD registry can be acquired by contacting the authors. To simplify the procedure of using the DAC board, the following environmental variables should be set:

- LabRADHost = localhost.
- LabRADNode = EPR.
- LabRADPassword = password.
- LabRADPort = 7682.

The HDL code used for the DAC board FPGA was version 10, as developed by John Martinis [36]. The Python scripts used to communicate with the DAC board are in-house software extensively modified from developments by Daniel Sank from the Martinis group, and can be acquired by contacting the authors.

B.2. Waveform generation

The Python scripts that communicate with the DAC board allow arbitrary waveforms to be generated on-the-fly. These can be based on analytical descriptions or specified with arbitrary time resolution. Fig. B1 shows an example: this pulse sequence generates the waveform shown in Fig. 4 (Section 3.1).

The function "`make_highres_waveform(list, resolution)`" can be called with a list of tuples that define (1) the type of pulse, (2) the phase of the pulse, and (3) the length of the pulse or delay. The first parameter can be "`rect`" (rectangular pulse), "`delay`", or "`function`" (defined by a function – here a lambda (i.e. inline) function giving an analytical expression for the pulse waveform). A rectangular pulse uses the second argument to define the pulse phase, which can be either "`x`", "`y`", "`−x`", "`−y`" or any angle between 0° and 360° (Fig. B1, lines 2 and 3). The third parameter defines the length of a pulse in units of seconds. In case of a delay, the second parameter defines its length. If the pulse type "*function*" is chosen, the second parameter is a function that defines the pulse shape as a function of time; here we employ lambda (inline) functions to generate analytically described functions that can be edited on-the-fly. Fig. B1 shows a triangular pulse (line 5), a Gaussian pulse (line 7), a truncated sinc pulse (line 9) and an adiabatic rapid passage sech/tanh pulse (line 11) as examples. The parameter "resolution" defines the time resolution for the pulse sequence – 40 ps in this case – that can be arbitrarily chosen.

```
1   wave = p.make_highres_waveform([
2       ('rect','x',50e-9),('delay',10e-9),('rect','-x',50e-9),('delay',10e-9),
3       ('rect','y',50e-9),('delay',10e-9),('rect','-y',50e-9),
4       ('delay',50e-9),
5       ('function', lambda x: (1-x)/2,100e-9),('function', lambda x: (x+1)/2,100e-9),
6       ('delay',50e-9),
7       ('function', lambda x: exp(-(x/0.3)**2),200e-9),
8       ('delay',50e-9),
9       ('function', lambda x: sin(x*5*pi+200e-9)/(x*5*pi+200e-9),200e-9),
10      ('delay',50e-9),
11      ('function',lambda x: sech(6*x)**(1+6j),200e-9)
12      ],resolution = 4e-11)
13
14  p.digitize(wave)
```

Fig. B1. Code that generates a pulse sequence – in this case a composite pulse comprising 4 rectangular pulses of different phases, a triangular pulse, a Gaussian pulse, a truncated sinc pulse, and an adiabatic rapid passage sech/tanh pulse.

The function "`digitize (wave)`" (line 14) takes the desired waveform as an argument, filters it with a 1 GHz Gaussian bandpass and down-samples it to a 1 ns time resolution. The previously acquired calibration parameters (Appendix C.2) and transfer function calibration (Appendix C.3) are applied, the waveform is translated into commands for the DAC board, transferred to the DAC board, and synthesized as described in Appendix C.1.

The language for pulse programming was kept simple to maximize user-friendliness. Arbitrary pulse shapes can be generated within a fraction of a second, and simple loops can be set up to perform two dimensional experiments, such as the T_2 experiment and coherence test presented in Section 3.1.

Appendix C. Digitization and synthesizer calibration

Descriptions of the algorithms used to generate, capture, as well as correct and calibrate arbitrary waveforms are given in this appendix.

C.1. Digitization and waveform generation

To digitize and generate an arbitrary waveform with the AWG from analytical descriptions, the desired waveform is defined with arbitrary length and resolution, then filtered with a 1 GHz Gaussian bandpass filter and down-sampled to a 1 ns time resolution to match the resolution of the DAC board. The IQ mixer calibration (Appendix C.2) as well as the transfer function calibration (Appendix C.3) are applied to take hardware imperfections into account and match the desired waveform as closely as possible. Subsequently, the waveform is translated into commands for the DAC board and transferred to the system. The following describes this procedure:

1. Define a desired waveform of arbitrary length and resolution, $w(t)$.
2. Filter with 1 GHz Gaussian: $w(t) * e^{-\left(\frac{t}{1\text{ns}}\right)^2}$.
3. Reduce bandwidth to 1 GHz: $w_i = \int_0^\infty w(t)\delta(t - t_i)\mathrm{d}t$ for t_i in 1 ns, 2 ns, ..., pulselength.
4. Apply IQ mixer calibration (Appendix C.2).
5. Apply transfer function correction (Appendix C.3).
6. Translate w_i to DAC board commands.
7. Transfer waveform to DAC board.

where "$*$" indicates time-domain convolution.

C.2. IQ mixer calibration

The IQ mixer used for waveform synthesis exhibits three correctable imperfections:

1. An amplitude imbalance between the two channels, i.e. "parity imbalance."
2. The phase angle between the two channels is not necessarily 90°.
3. Microwave leakage occurs when no voltage is applied to both channels.

To correct for all three of these issues, a plane wave U_{in} is generated via the DAC board, mixed with the reference oscillator via the IQ mixer, and the output waveform U_{out} is captured on the sampling oscilloscope. In general, where an input waveform, U_{in}, has the form

$$U_{in}(t) = \rho_{in}(t)e^{i\phi_{in}(t)} \tag{7}$$

where ρ_{in} and ϕ_{in} are real numbers giving, respectively, the amplitude and phase modulation of the waveform, the amplitude and phase of the output waveform will be altered according to equations

$$\Re[U_{out}(t)] = (1 + B_\Re)A_{\Re}\rho_{in}(t) \cos[\phi_{in}(t) + \vartheta_\Re] + C_\Re \tag{8}$$

$$\Im[U_{out}(t)] = (1 + B_\Im)A_{\Im}\rho_{in}(t) \sin[\phi_{in}(t) + \vartheta_\Im] + C_\Im \tag{9}$$

as a result of these imperfections [47]. The A_R and A_I represent the output parity imbalance, the B_R and B_I represent the input parity imbalance, the ϑ_R and ϑ_I denote a phase shift (arising from slightly different path lengths in each channel), and the C_R and C_I represent the DC offset of the real (Eq. (8)) and imaginary (Eq. (9)) components of the output waveform.

Specifically, after outputting a plane-wave U_{out}, the real and imaginary components of the output waveform, which are captured on the sampling scope, are fit to equations (Eq. (8)) and (Eq. (9)), respectively, as a function of the input phase.

Once these calibration parameters have been determined, one can solve Eqs. (8) and (7) with a standard zero-finding algorithm to determine the input values of ρ_{in} and ϕ_{in} needed to yield any desired output amplitude and phase (i.e. $|U_{out}|$ and angle (U_{out})), respectively. This corrects the amplitude and phase of the output waveform. In particular, the microwave leakage is corrected by subtracting the terms C_R and C_I from the input waveform's real and imaginary components, respectively. This applies a voltage to each channel of the mixer to minimize microwave leakage at the

output and allows for an isolation of more than 50 dB post amplification.

The IQ mixer used for detection exhibits the same issues as the mixer used for waveform synthesis. Therefore, an analogous calibration procedure can be applied, the difference being that non-linearities are accounted for in post processing.

C.3. Transfer function calibration

To maximize the fidelity with which pulses are generated, the transfer function of the spectrometer can be taken into account as a final step by capturing the generated waveform and comparing it to the desired pulse shape. Linear response theory states that the output waveform, $p_{out}(t)$, can be described as a convolution of the input waveform, $p_{in}(t)$, with the impulse response of the system – i.e. the inverse Fourier transform of the transfer function, $T(f)$, of the system. We represent this as

$$p_{out}(t) = p_{in}(t) * \mathcal{F}^{-1}\{T(f)\}(t) \tag{10}$$

where $\mathcal{F}^{-1}\{\ldots\}$ represents the inverse Fourier transform and $*$ again represents a time-domain convolution. After Fourier transformation, the transfer function in frequency space can be found, following from

$$\mathcal{F}\{p_{out}(t)\}(f) = \mathcal{F}\{p_{in}(t)\}(f)T(f) \tag{11}$$

The transfer function, $T(f)$, can be subsequently applied to the initial waveform function to generate the desired waveform $p_{cor}(t)$ as described in the procedure below.

Instead of using the desired output pulse to determine the transfer function, a 1 ns rectangular pulse on each DAC channel can be used to determine the impulse response function of the spectrometer and the transfer functions for both channels T_A (corresponding to a real 1 ns pulse) and T_B (corresponding to an imaginary 1 ns pulse) are added to determine the total transfer function, T. The procedure is described below. This procedure was not utilized in the experiments presented, but offers opportunity for future applications.

Generate 1 ns square pulse $p_{in}(t)$ on DAC channel A and capture impulse response $p_{out}(t)$ on sampling oscilloscope

1. Fourier transform the generated waveform to yield $\mathcal{F}\{p_{in}(t)\}(f)$ and the impulse response to yield $\mathcal{F}\{p_{out}(t)\}(f)$.
2. Find the transfer function $T_A(f) = \frac{\mathcal{F}\{p_{out}(t)\}(f)}{\mathcal{F}\{p_{in}(t)\}(f)}$.
3. Repeat steps 1 through 3 with DAC channel B to find total transfer function $T(f) = T_A + T_B$.
4. Find Fourier transform of corrected output waveform.

$$\mathcal{F}\{p_{cor}\}(f) = \frac{\mathcal{F}\{p_{out}(t)\}(f)}{\mathcal{F}\{p_{in}(t)\}(f)}$$

1. Inverse Fourier transform corrected output waveform to yield. $\mathcal{F}^{-1}\{\mathcal{F}\{p_{cor}(t)\}(f)\}(t) = p_{cor}(t)$

Appendix D. Waveform capturing

To be able to generate arbitrary waveforms with a defined phase, the absolute phase of the generated pulse needs to be determined, so that a calibration procedure can be applied. Any microwave pulse or reflection of the resonator in the system can be detected with absolute phase information by employing the second channel of the sampling oscilloscope, which is fed with the attenuated output of the microwave source. The phase of each data point of the signal channel is compared to the phase of the constant amplitude reference wave. The procedure is described

below, where $\mathcal{H}$ gives the Heaviside step function ($\mathcal{H}(x) = 1$ for $x > 0$ and $\mathcal{H}(x) = 0$ for $x < 0$).

1. Simultaneously capture plain microwave carrier $c_{ref}(t)$ and waveform to be analyzed $c_{cap}(t)$.
2. Generate analytic signal and apply bandpass filter to reduce noise:

$$\mathcal{F}\{c_{ref}(t)\}(f)\mathcal{H}(f)\mathcal{H}(f - 10\text{GHz})\mathcal{F}\{c_{ref}\}(f)$$

$$\mathcal{F}\{c_{cap}(t)\}(f)\mathcal{H}(f)\mathcal{H}(f - 10\text{GHz})\mathcal{F}\{c_{cap}\}(f) \text{ with } \mathcal{F}\{\ldots\}$$
$$= \int_{-\infty}^{\infty} e^{i2\pi ft}\ldots \mathrm{d}t$$

1. Determine absolute phase: $c_{cap,\phi}(t) = c_{cap}(t)\frac{|c_{ref}(t)|}{c_{ref}(t)}$.
2. Apply bandpass filter to reduce noise:

$$\mathcal{F}\{c_{cap,\phi}(t)\}(f)\mathcal{H}(f)\mathcal{H}(f - 2\text{GHz})\mathcal{F}\{c_{cap}(t)\}(f)$$

References

[1] P. Fajer, Electron spin resonance spectroscopy labeling in peptide and protein analysis, Encyclopedia Anal. Chem. (2006) 5725–5761.
[2] O. Schiemann, T.F. Prisner, Long-range distance determinations in biomacromolecules by EPR spectroscopy, Q. Rev. Biophys. 40 (2007) 1–53.
[3] J.A. Weil, J.R. Bolton, Electron Paramagnetic Resonance, John Wiley & Sons, Inc., Hoboken, New Jersey, 2007.
[4] R.T. Weber, ELEXSYS E580 User's Manual, Bruker BioSpin Corporation, Billerica, MA, 2005.
[5] J.P. Hornak, J.H. Freed, Spectral rotation in pulsed ESR spectroscopy, J. Magn. Reson. 67 (1986) 501–518.
[6] J.S. Hodges, J.C. Yang, C. Ramanathan, D.G. Cory, Universal control of nuclear spins via anisotropic hyperfine interactions, Phys. Rev. A 78 (2008) 010303.
[7] Y. Zhang, C. Ryan, R. Laflamme, J. Baugh, Coherent control of two nuclear spins using the anisotropic hyperfine interaction, Phys. Rev. Lett. 107 (2011) 170503.
[8] T.E. Skinner, K. Kobzar, B. Luy, M.R. Bendall, W. Bermel, N. Khaneja, S.J. Glaser, Optimal control design of constant amplitude phase-modulated pulses: application to calibration-free broadband excitation, J. Magn. Reson. 179 (2006) 241–249.
[9] J. Pauly, P. Le Roux, D. Nishimura, a. Macovski, Parameter relations for the Shinnar–Le Roux selective excitation pulse design algorithm [NMR imaging], IEEE Trans. Med. Imaging 10 (1991) 53–65.
[10] N. Khaneja, T. Reiss, C. Kehlet, T. Schulte-Herbrüggen, S.J. Glaser, Optimal control of coupled spin dynamics: design of NMR pulse sequences by gradient ascent algorithms, J. Magn. Reson. 172 (2005) 296–305.
[11] A. Doll, S. Pribitzer, R. Tschaggelar, G. Jeschke, Adiabatic and fast passage ultra-wideband inversion in pulsed EPR, J. Magn. Reson. 230 (2013) 27–39.
[12] P.E. Spindler, S.J. Glaser, T.E. Skinner, T.F. Prisner, Broadband inversion PELDOR spectroscopy with partially adiabatic shaped pulses, Angew. Chem. 52 (2013) 3425–3429.
[13] P.E. Spindler, Y. Zhang, B. Endeward, N. Gershernzon, T.E. Skinner, S.J. Glaser, T.F. Prisner, Shaped optimal control pulses for increased excitation bandwidth in EPR, J. Magn. Reson. 218 (2012) 49–58.
[14] G. Jeschke, Distance measurements in the nanometer range by pulse EPR, ChemPhysChem 3 (2002) 927–932.
[15] L. Kevan, L.D. Kisper, Electron Spin Double Resonance Spectroscopy, Interscience, New York, NY, 1976.
[16] J. Hyde, J. Chien, J. Freed, Electron–electron double resonance of free radicals in solution, J. Chem. Phys. 48 (1968).
[17] Y. Chiang, A. Costa-Filho, J. Freed, Dynamic molecular structure and phase diagram of DPPC-cholesterol binary mixtures: a 2D-ELDOR study, J. Phys. Chem. B 111 (2007) 11260–11270.
[18] Y.-W. Chiang, A.J. Costa-Filho, B. Baird, J.H. Freed, 2D-ELDOR study of heterogeneity and domain structure changes in plasma membrane vesicles upon cross-linking of receptors, J. Phys. Chem. B 115 (2011) 10462–10469.
[19] P. Hofer, H. Grupp, H. Nebenfuhr, M. Mehring, Hyperfine sublevel correlation (HYSCORE) spectroscopy: a 2d ESR investigation of the square acid radical, Chem. Phys. Lett. 132 (1986) 279–282.
[20] R. Szosenfogel, D. Goldfarb, Simulations of HYSCORE spectra obtained with ideal and non-ideal pulses, Mol. Phys. 95 (1998) 1295–1308.
[21] P.P. Borbat, J.H. Freed, Multiple-quantum ESR and distance measurements, Chem. Phys. Lett. 313 (1999) 145–154.
[22] G.a. Rinard, R.W. Quine, R. Song, G.R. Eaton, S.S. Eaton, Absolute EPR spin echo and noise intensities, J. Magn. Reson. 140 (1999) 69–83.
[23] S.K. Misra, J.H. Freed, Distance measurements: continuous-wave (CW)- and pulsed dipolar EPR, Multifrequency Electron Paramagnetic Reson.: Theory Appl. (2011) 545–588.

[24] B.D. Armstrong, S. Han, A new model for Overhauser enhanced nuclear magnetic resonance using nitroxide radicals, J. Chem. Phys. 127 (2007) 104508.
[25] M.-T. Turke, M. Bennati, Saturation factor of nitroxide radicals in liquid DNP by pulsed ELDOR experiments, Phys. Chem. Chem. Phys. 13 (2011) 3630–3633.
[26] C.J. Bardeen, V.V. Yakovlev, K.R. Wilson, S.D. Carpenter, P.M. Weber, W.S. Warren, Feedback quantum control of molecular electronic poplation transfer, Chem. Phys. Lett. 280 (1997) 151–158.
[27] R. Crepeau, A. Dulic, J. Gorcester, T. Saarinen, J. Freed, Composite pulses in time-domain ESR, J. Magn. Reson. 84 (1989) 184–190.
[28] R.H. Pursley, J. Kakareka, G. Salem, N. Devasahayam, S. Subramanian, R.G. Tschudin, M.C. Krishna, T.J. Pohida, Stochastic excitation and Hadamard correlation spectroscopy with bandwidth extension in RF FT-EPR, J. Magn. Reson. 162 (2003) 35–45.
[29] N. Devasahayam, R. Murugesan, K. Matsumoto, J.B. Mitchell, J.a. Cook, S. Subramanian, M.C. Krishna, Tailored sinc pulses for uniform excitation and artifact-free radio frequency time-domain EPR imaging, J. Magn. Reson. 168 (2004) 110–117.
[30] M. Silver, R. Joseph, D. Hoult, Selective spin inversion in nuclear magnetic resonance and coherent optics through an exact solution of the Bloch-Riccati equation, Phys. Rev. A 31 (1985) 2753–2755.
[31] M. Garwood, L. DelaBarre, The return of the frequency sweep: designing adiabatic pulses for contemporary NMR, J. Magn. Reson. 153 (2001) 155–177.
[32] B. Blümich, Q. Gong, E. Byrne, M. Greferath, NMR with excitation modulated by Frank sequences, J. Magn. Reson. 199 (2009) 18–24.
[33] T.W. Borneman, D.G. Cory, Bandwidth-limited control and ringdown suppression in high-Q resonators, J. Magn. Reson. 225 (2012) 120–129.
[34] R.C. Bialczak, M. Ansmann, M. Hofheinz, E. Lucero, M. Neeley, A.D. O'Connell, D. Sank, H. Wang, J. Wenner, M. Steffen, A.N. Cleland, J.M. Martinis, Quantum process tomography of a universal entangling gate implemented with Josephson phase qubits, Nature Phys. 6 (2010) 409–413.
[35] G.a. Rinard, R.W. Quine, R. Song, G.R. Eaton, S.S. Eaton, Absolute EPR spin echo and noise intensities, J. Magn. Reson. 140 (1999) 69–83.
[36] J.M. Martinis, Superconducting phase qubits, Quantum Inf. Process. 8 (2009) 81–103.
[37] T. Maly, F. MacMillan, K. Zwicker, N. Kashani-Poor, U. Brandt, T.F. Prisner, Relaxation filtered hyperfine (REFINE) spectroscopy: a novel tool for studying overlapping biological electron paramagnetic resonance signals applied to mitochondrial complex I, Biochemistry 43 (2004) 3969–3978.
[38] G.R. Eaton, S.S. Eaton, R.W. Quine, D. Mitchell, V. Kathirvelu, R.T. Weber, A signal-to-noise standard for pulsed EPR, J. Magn. Reson. 205 (2010) 109–113.
[39] A. Tannús, M. Garwood, Adiabatic pulses, NMR Biomed. 10 (1997). 423-34.
[40] J. Cavanagh, W.J. Fairborther, A.G. Palmer, N.J. Skelton, M. Rance, Protein NMR Spectroscopy: Principles and Practice, second ed., Academic Press, Waltham, MA, 2006.
[41] S. Saxena, J.H. Freed, Theory of double quantum two-dimensional electron spin resonance with application to distance measurements, J. Chem. Phys. 107 (1997) 1317.
[42] E. Stejskal, J. Schaefer, Comparisons of quadrature and single-phase fourier transform NMR, J. Magn. Reson. 14 (1974) 160–169.
[43] R. Crepeau, A. Dulic, J. Gorcester, T. Saarinen, J. Freed, Composite pulses in time-domain ESR, J. Magn. Reson. 84 (1989) 184–190.
[44] G. Jeschke, A. Schweiger, Matched two-pulse electron spin echo envelope modulation spectroscopy, J. Chem. Phys. 105 (1996) 2199–2211.
[45] M. Tseitlin, R.W. Quine, G.A. Rinard, S.S. Eaton, G.R. Eaton, Digital EPR with an arbitrary waveform generator and direct detection at the carrier frequency, J. Magn. Reson. 213 (2011) 119–125.
[46] K. Kobzar, B. Luy, N. Khaneja, S.J. Glaser, Pattern pulses: design of arbitrary excitation profiles as a function of pulse amplitude and offset, J. Magn. Reson. 173 (2005) 229–235.
[47] S. Sabah, T.U. Berlin, R. Lorenz, D. Zeuthen, Design and calibration of IQ-mixers, in: Proceedings of the European Particle Accelerator Conference 1998, Sweden, 1998, pp. 1589–1591.